Final Summary of Research
NAG 3-2397
Transition from Pool to Flow Boiling – The Effect of Reduced Graviy

Vijay K. Dhir, Principal Investigator
Mechanical and Aerospace Engineering Department
University of California, Los Angeles
Los Angeles, CA 90095-1597

SUMMARY

Applications of boiling heat transfer in space can be found in the areas of thermal management, fluid handling and control, power systems, on-orbit storage and supply systems for cryogenic propellants and life support fluids, and for cooling of electronic packages for power systems associated with various instrumentation and control systems. Recent interest in exploration of Mars and other planets, and the concepts of in-situ resource utilization on Mars highlights the need to understand the effect of gravity on boiling heat transfer at gravity levels varying from $1 \geq g/g_e \geq 10^{-6}$.

The objective of the proposed work was to develop a mechanistic understanding of nucleate boiling and critical heat flux under low and micro-gravity conditions when the velocity of the imposed flow is small. For pool boiling, the effect of reduced gravity is to stretch both the length scale as well as the time scale for the boiling process. At high flow velocities, the inertia of the liquid determines the time and the length scales and as such the gravitational acceleration plays little role. However, at low velocities and at low gravity levels both liquid inertia and buoyancy are of equal importance. At present, we have little understanding of the interacting roles of gravity and liquid inertia on the nucleate boiling process. Little data that has been reported in the literature does not have much practical value in that it can not serve as a basis for design of heat exchange components to be used in space.

Both experimental and complete numerical simulations of the low velocity, low-gravity nucleate boiling process were carried out. A building block type of approach was used in that first the growth and detachment process of a single bubble and flow and heat transfer associated with the sliding motion of the bubble over the heater surface after detachment was studied. Liquid subcooling and flow velocity were varied parametrically. The experiments were conducted at 1 g_e, while varying the orientation of surface with respect to the gravity vector. In the laboratory experiments, holographic interferometry was used to obtain data on velocity and temperature fields associated with a bubble prior to, and after detachment and during sliding motion. A test rig for conducting experiments in the KC-135 was developed, but experiments could not be conducted due to the unavailability of the aircraft prior to completion of the project. Numerical simulations modeling the micro and macro regions of the bubble were carried out in three dimensions. The results of the experiments were used to validate analytical/numerical models.

1. INTRODUCTION

Boiling is known to be a very efficient mode of heat transfer, and as such, it is employed in component cooling and in various energy conversion systems. For space applications, boiling is the heat transfer mode of choice, since for a given power rating the size of the components can be significantly reduced. For any space mission, the size and, in turn, the weight of the components plays an important role in the economics of the mission.

Applications of boiling heat transfer in space can be found in the areas of thermal management, fluid handling and control, and power systems. For power systems based on the Rankine cycle (a representative power cycle), key issues that need to be addressed are the magnitude of nucleate boiling heat transfer coefficient and the critical heat flux under low-gravity conditions. Knowledge of nucleate boiling heat transfer coefficient is necessary to determine the overall resistance for transfer of heat from a heat source to a heat sink. The critical heat flux represents the upper limit for safe heat removal since for heat fluxes greater than critical heat flux the surface will be covered with a vapor film which in turn will result in a rapid rise in the temperature or failure of the component.

Understanding and quantification of boiling heat fluxes at low-gravity, low velocity boiling conditions are also important for other space power systems such as thermionic reactors operating under transient conditions (see e.g., von Arx and Dhir, 1993). An assessment of cooling of electronic packages for power supply systems associated with various instrumentation and control systems is dependent on a knowledge of boiling heat transfer. Additionally, design and development of safe operating procedures for on-orbit storage and supply systems for cryogenic propellants and life support fluids requires quantitative data for boiling heat transfer under long duration of microgravity conditions.

A key element of the future space vehicles supporting Human Exploration and Development of Space (HEDS) missions is the use of cryogenic liquids for the propulsion, power, and life support systems. In-situ resource utilization (ISRU) has been shown to reduce, significantly, the earth launch mass of lunar and Mars missions. Central to the ISRU theme is the production, liquification and storage of oxygen and methane as propellants, oxygen as a reactant for localized power generation, and for crew life support. These systems can be expected to operate under gravity levels varying from $1 \geq g/g_e \geq 10^{-6}$. Thus necessitating an understanding of boiling heat transfer that includes scaling with respect to magnitude of gravity.

The cryogenic liquid storage and propellant feed system (CSPFS) is required to provide propellant during engine burn in controlled amounts and at specified conditions. Themohydraulic oscillations due to boiling of saturated or subcooled cryogenic propellant, coupled with transient heat and momentum transport may significantly affect the flow rate during engine burns. Such transients can lead to instability of the fluid structure system. A meaningful stability analysis of such a system will require quantitative knowledge of flow boiling heat transfer coefficient as a function of wall superheat and of the limiting conditions.

At present we have little understanding of this important mode of heat transfer at low gravity levels and under low flow velocity conditions, and we have no correlations or models which a designer can use to design efficient heat exchange equipment with any level of

confidence. The basic study conducted in this work represented a first step in developing a mechanistic model for flow boiling heat transfer under low gravity conditions.

2. RESEARCH ACCOMPLISHMENTS

Results of both experimental and numerical studies conducted under this project are described in the following.

2.1 Experiments

The objective of the experiments was to provide, in a very clean manner, the information that is needed to develop a mechanistic model for nucleate boiling heat flux as a function of wall superheat, including maximum heat flux at low flow velocities parallel to the heater, and at gravity levels varying from $1 \leq /g_e \leq 10^{-6}$. The experiments were conducted at earth normal gravity.

The flow loop shown in Fig. 1 consists of storage tanks, pump, flowmeter, preheater, test section with developing section for hydrodynamic entry length, and tubing network. The test section is mounted on a vertical stand with a horizontal axis to facilitate rotation about that axis. To facilitate rotation, stainless steel hose assemblies are used to connect the test section to the rest of the loop.

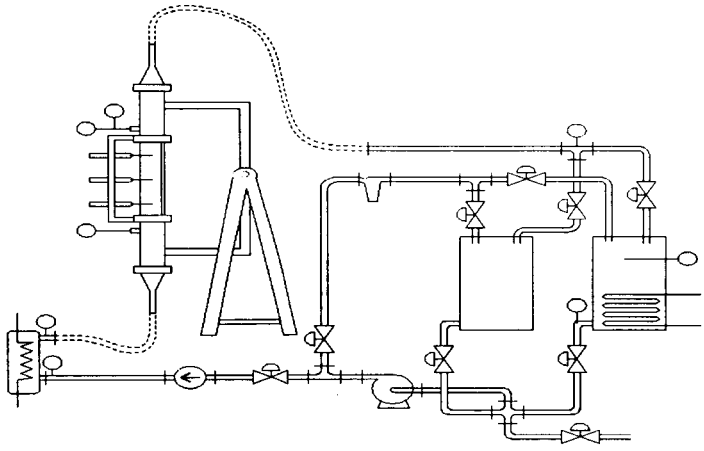

Figure 1: Schematic of Flow Boiling Experiment Set Up.

The test section is designed for a rectangular flow section (20 × 20 × 300 mm) with pyrex glass on three sides mounted on a stainless steel frame to allow visual observations and optical measurements. On the fourth side, Silicon wafers were mounted on a phenolic G10 base bonded to it by GE two part silicone RTV60. Thermocouples attached to traversing micrometers are mounted from the opposite end to measure the thermal boundary layer in the liquid. Fig. 2a shows the cross-sectional view of the test chamber.

The test surface is made up of three rectangular (19mm × 99.9mm) polished Silicon strips placed in series. The reasoning behind choosing the Silicon strips as the test surface are as follows: 1) Silicon wafer can be manufactured using commercial techniques to give an excellent

surface finish, which helps in avoiding nucleation of spurious bubbles on the surface and 2) well established MEMS machining techniques can be used to fabricate the desired single cavity needed for the experiments.

Of the three strips mounted on the G10 base, the middle strip contains a deep reaction ion etched 10 micron square cavity that is 50 micron deep at the geometric center. The etched wafers were commercially obtained from MCNC. Originally, the wafers supplied were circular, but they were diced into required rectangular dimensions at the UCLA Micromachining Laboratory.

The upstream, downstream and middle strips have two rows of precision strain gages bonded along the length at the back. The strain gages are used as heating elements (Fig. 2b). These thin film strain gage heaters were obtained from Measurements Group, NJ. Each strain gage heater is 10 mm x 7.5 mm with an effective heated portion of 6.5 mm x 6.5 mm, the remaining portions being used for soldering leads. The resistance of each heater element is 120 Ω and it could supply approximately 40W of power.

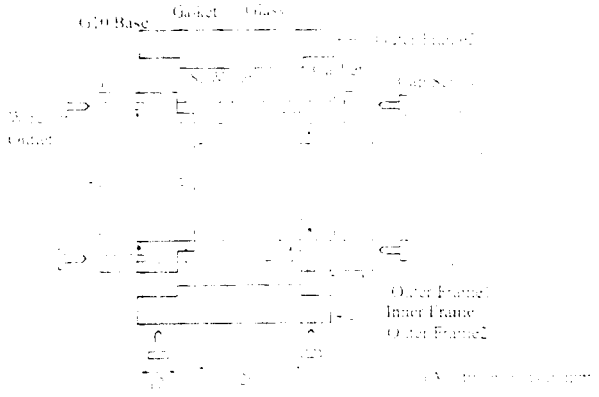

(a) Cross View of Test Section

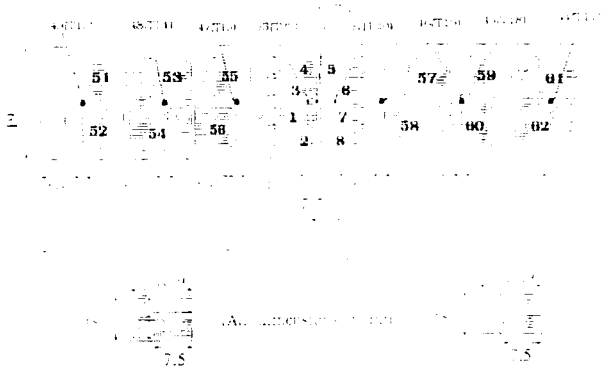

(b) Positions of Strain Gage Heaters & Thermocouple on Wafer Back.

Figure 2: Schematic of Test Section and Heater.

Thermocouples used in the experiment are of K-type (Chromel-Alumel). Grounded sheath thermocouples of outer dia 1.5 mm were used to measure the temperature of flowing water at different junctions of the loop, namely the tanks, inlet and outlet of the preheater, and inlet and outlet of the test section. Thermal profile in the liquid above the test surface was measured with three sheathed thermocouples of diameter 0.25mm, attached to traversing micrometers. Temperature of the test surface was measured with thermocouples bonded to the back of the wafer surface along the center line.

Complete details of the experimental procedure, data reduction, and uncertainty in data are given in Maity (2000).

Bubble dynamics was studied for water upflow velocities of about 0.076, 0.14, and 0.25 m/s for horizontal (0°), vertical (90°), inclined facing upwards (30°, 45°, 60°) as well as for an inclined facing downward (135°) orientations of the test surface. The test liquid was nearly saturated, but in a few cases the liquid subcooling was parametrically varied. In the following typical results for various inclinations are described. Thereafter main observations from all of the data are summarized.

2.1.1 Horizontal Surface (0°)

Photographs for one ebbulition cycle on the cavity are shown in Fig. 3. The time sequence of the video frames is from left to right and from top to bottom. Designation of upstream and downstream contact angles, the bubble base diameter, and major and minor bubble axis is given in an enlarged photograph of a typical bubble shown in Fig. 4. It seen from Fig. 3 that as the bubble grows, the bubble base diameter also increases at first. Initially the bubble is symmetrical about an axis perpendicular to the heater surface. However with increase in bubble size, it becomes inclined in the direction of flow and subsequent growth of the bubble is unsymmetrical. In the photographs reflection of the bubble on the test surface is also seen. The apparent neck between the bubble and its reflection is an optical effect, which depends on the angle at which photograph is taken. The different bubble growth cycles were chosen from the movie files, and were analyzed in detail. Figure 5 shows as a function of time the bubble diameter, bubble velocity, and bubble base diameter obtained from movies. The bubble diameter is defined as the diameter of a sphere that has the same volume as the bubble. It is found that up to 13 ms the bubble grows on the cavity. Thereafter the bubble begins to slide along the heater surface. The sliding motion lasts for another 10 ms before the bubble lifts off from the surface. Bubble growth continues during the sliding phase and the bubble sliding velocity increases until bubble lifts-off from the surface. During the bubble growth at the cavity, the bubble base diameter also increases and attains a maximum value prior to bubble departure. Thereafter the base diameter remains constant at its maximum value during the sliding phase before it rapidly decreases as the bubble starts to lift off from the surface.

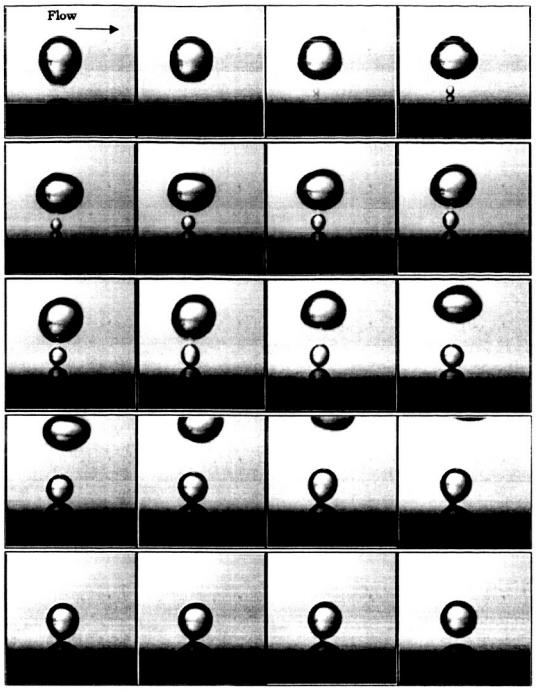

Figure 3: Growth Cycle for Horizontal Surface; V = 0.076 m/s, ΔT_{wall}= 5.3°C, ΔT_{sub}= 0.2°C,

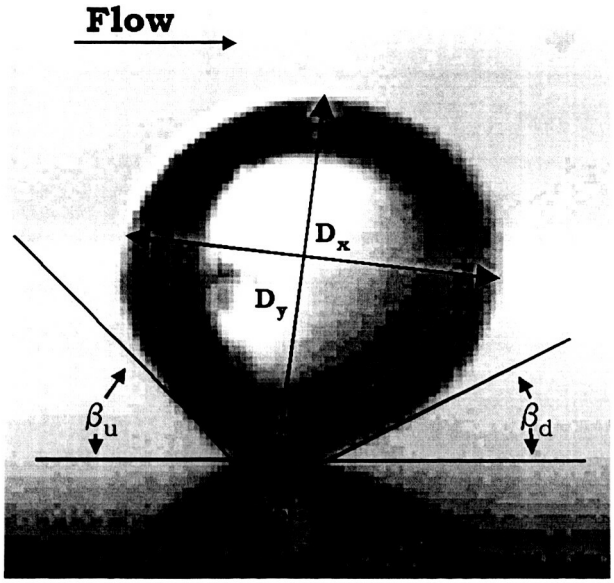

Figure 4: Typical Bubble under Flow Conditions.

Similar results were obtained for other flow velocities. The bubble departure and lift off diameters and bubble velocity at lift off are plotted in Fig. 6. It is noted that for all velocities the bubble lift off diameter is larger than the departure diameter, although the difference between the two diminishes with increase in flow velocities. The lift off and departure diameters are comparable to the thickness of the hydrodynamic boundary layer as deduced from the temperature profiles. Both diameters decrease with flow velocity. The bubble velocity at lift off increases with flow velocity and is somewhat smaller than the free stream velocity.

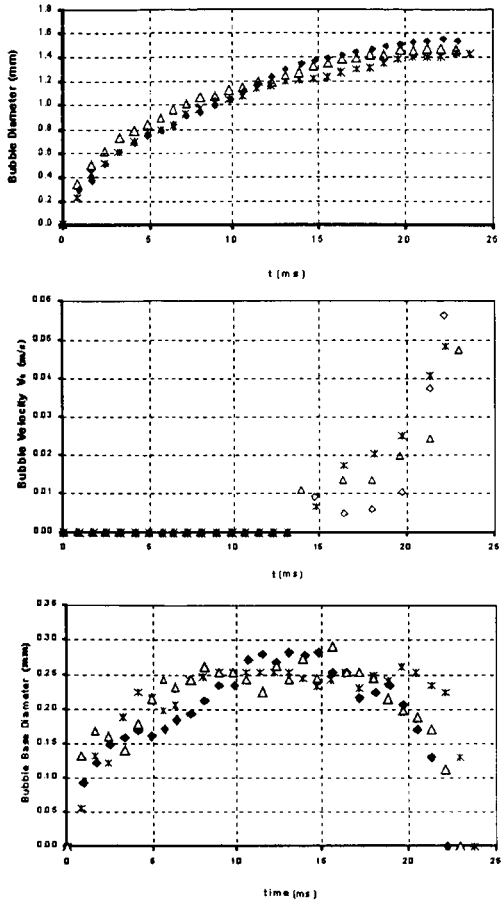

Figure 5: Bubble Growth Bubble Sliding Velocity and Base Diameter on Horizontal Surface V = 0.076 m/s, ΔT_{wall} = 5.3 °C. ΔT_{sub} = 0.2 °C.

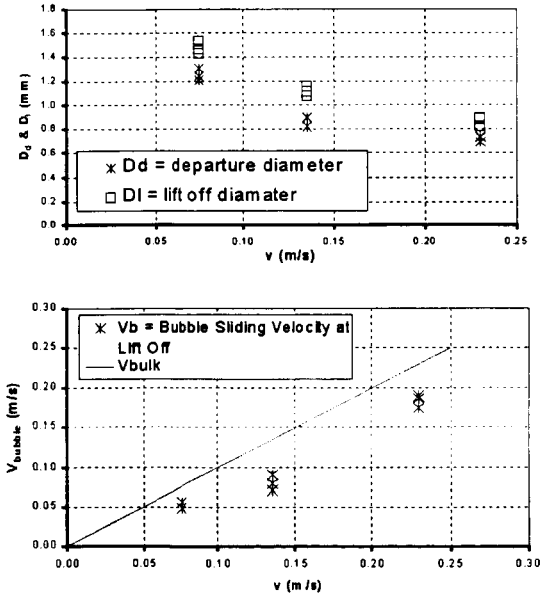

Figure 6: Effect of Bulk Liquid Velocity on Bubble Departure and Lift Off Diameter, Bubble Velocity at Lift Off.

2.1.2 Vertical Surface (90°)

Video pictures of one growth cycle of a bubble in vertical upflow of nearly saturated water (ΔT_{subs} = 0.3°C) at a flow velocity of 0.25 m/s are shown in Fig. 7. The wall superheat in this case was 5.9 ^{0}C. Bubble growth rate and bubble sliding velocity obtained from the video pictures such as those shown in Fig. 7 are plotted in Fig. 8. The bands around the data represent error bars. It is observed that the bubble grows at its nucleation site for 4 ms when it attains a diameter of 0.9 mm. Thereafter the bubble starts to slide and continues to grow. At 7 ms, its sliding velocity reaches around 0.28 m/s with diameter about 1.1 mm when it is observed to have lost contact with the surface. Subsequently, its diameter is also observed to have decreased leading to the conclusion that some condensation has occurred in the presence of subcooled liquid. At 10 ms, it is observed to have regained contact with the heater surface while its velocity is seen to have decreased to 0.19 m/s. Thereafter, it continues to grow as it slides and accelerates. Finally at around 55 ms, it lifts off from the surface into the liquid after attaining a diameter of 1.8 mm and sliding velocity of 0.4 m/s, never to return to the surface.

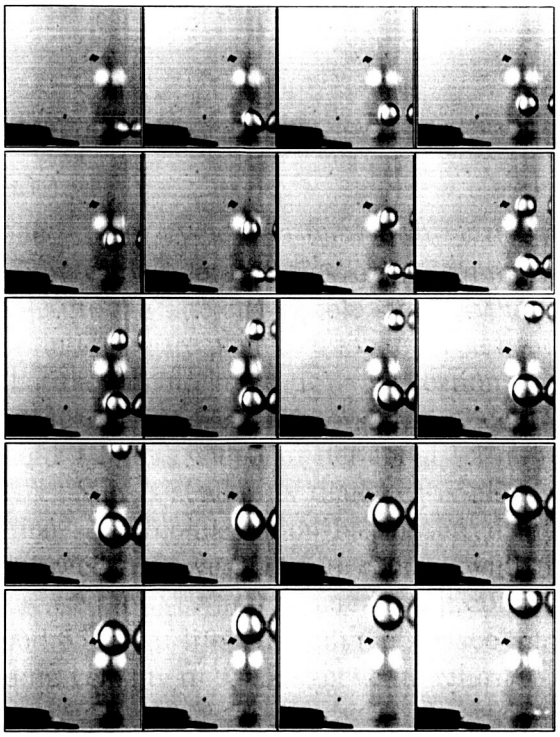

Figure 7: Growth Cycle for Vertical Surface, Upflow, (*near field view*); V = 0.025 m/s, ΔT_{wall}= 5.9°C, ΔT_{sub}= 0.3°C.

The effect of bulk liquid velocity on bubble departure and lift-off diameters and bubble sliding velocity at lift off is plotted in Fig. 9. As was the case for a horizontal surface, both the departure and lift off diameters decrease with bulk velocity. The sliding velocity at lift off is seen to increase with flow velocity. This velocity is found to be always higher than the bulk velocity. In comparison, although the bubble velocity at lift off for the horizontal surface increased with flow velocity it was always somewhat less than the bulk velocity. The sliding distance was also seen to increase with flow velocity. It was about 2 mm under pool boiling conditions and about 17 mm at a bulk velocity of 0.25 m/sec.

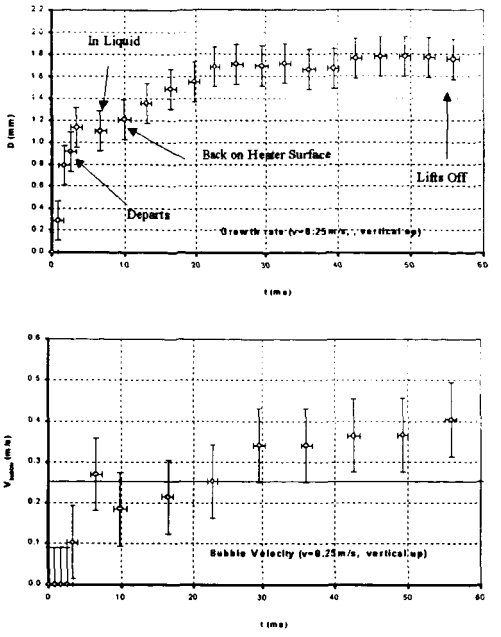

Figure 8: Growth Cycle and Velocity in a Typical Cycle, Vertical Surface, Upflow, V = 0.025 m/s, ΔT_{wall}= 5.9°C, ΔT_{sub}= 0.3°C.

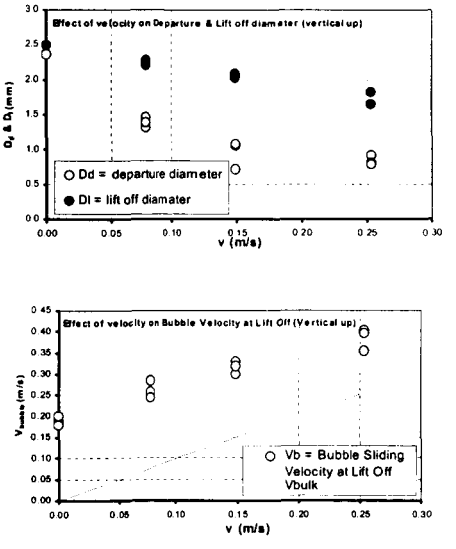

Figure 9: Effect of Bulk Liquid Velocity on Departure and Lift Off Diameter and Bubble Velocity at Lift Off (vertical up).

Similar data were obtained when the test surface was inclined at 30^0, 45^0, 60^0, and 135^0 (downward facing surface) with the horizontal.

Changing the heater surface orientation alters the magnitude of gravity both normal and parallel to the heater surface. The normal component of gravity decreases whereas the parallel component increases as the heater surface is rotated from 0^o (horizontal) to 90^o (vertical). In Fig. 10, the bubble diameter at departure is plotted as a function of bulk velocity for all of the heater angular positions studied in this work. The data for horizontal surface under pool boiling

conditions is not included because in this case any liquid drag acting on the bubble will be symmetrical about an axis normal to the heater. From the data plotted in Fig. 10, it is seen that for all cases bubble diameter at departure decreases with flow velocity and within the data scalter no distinguishable effect of gravity along the heater surface is seen. This suggests that **drag** on an asymmetrically growing bubble is probably balanced by surface tension acting in the opposite direction.

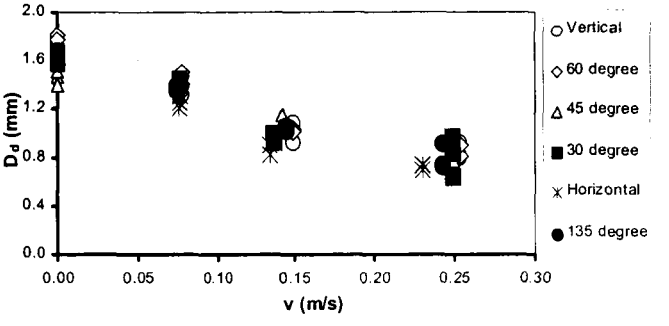

Figure 10: Effect of Bulk Liquid Velocity and Orientation on Departure Diameter.

Bubble lift off diameters for all the angular positions are plotted in Fig. 11. It is seen that although for all inclinations the bubble lift off diameters decrease with flow velocity, a distinct effect of orientation on bubble lift off diameter is observed. As the angle of inclination is increased, the component of buoyancy force normal to the heater surface decreases and finally completely vanishes for the vertical surface. It is interesting to note that bubble acquires a larger diameter before lift off when angle of inclination of the surface is increased. Since for a vertical surface no buoyancy force acts normal to the surface, another force (lift) must act on the bubble. This lift force results from the relative velocity difference between the bubble sliding along the heater surface and the bulk flow.

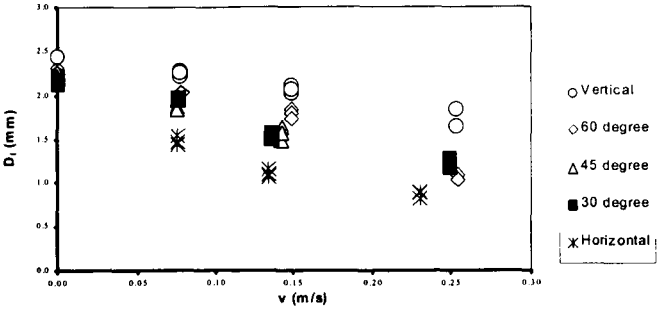

Figure 11: Effect of Bulk Liquid Velocity and Orientation on Lift Off Diameter.

The bubble velocity at lift off and bubble sliding distance as a function of bulk velocity are plotted in Fig. 12 and 13, respectively for different orientations of the test surface. Except for the horizontal surface and the surface inclined at 30°, the bubble velocity at lift-off is at least equal to or greater than the bulk velocity. Even for the horizontal surface the bubble velocity at lift-off is not much smaller than the bulk velocity. Increased velocity results from the hydrostatic head difference that exists between the back and front portions of the bubble in a gravitational field. It appears that faster the bubble moves relative to the bulk liquid layer the higher the lift force

away from the heater. The lift force also increases with size of the bubble. The distance traveled by the bubble prior to lift off is observed to increase with the relative velocity the bubble is required to attain before lift off.

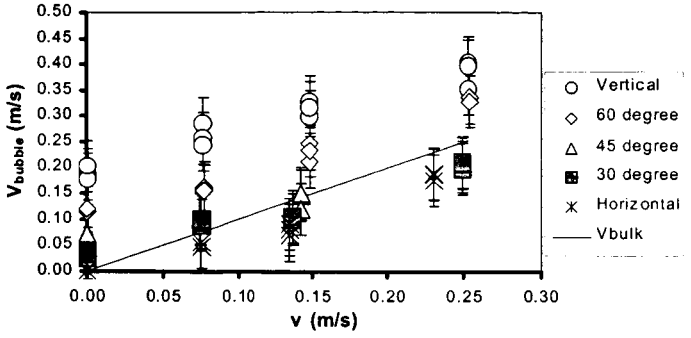

Figure 12: Effect of Bulk Liquid Velocity and Orientation on Bubble Velocity at Lift Off.

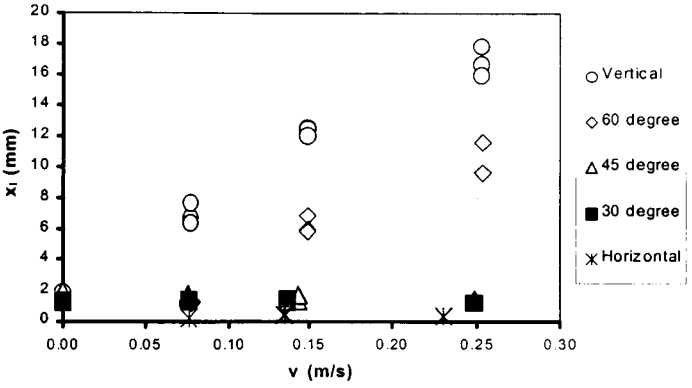

Figure 13: Effect of Bulk Liquid Velocity and Orientation on Bubble Sliding Distance Before Lift Off.

During the growth and sliding motion of the bubble the upstream contact angles were always larger than the downstream contact angles. However, no distinct effect of magnitude of velocity or angular position of the heater on the upstream and downstream contact angles was found.

2.2 Numerical Model

This section presents the 3D computational model used in this study which was originally developed for pool boiling by Son *et al.* (1999). In this model, the computational domain is divided into the micro region and macro region. The micro region is a thin film that lies underneath the bubble, whereas the macro region consists of the bubble and the liquid surrounding the bubble. The governing equations for mass, momentum and energy are numerically solved for each of these two domains. Only half of the bubble is considered since the bubble is symmetric about the flow direction. A staggered grid is used in the finite difference scheme. To accelerate computation, multigrid and block correction methods are used. The discretized equations are solved by a line-by-line TDMA (Tri-diagonal Matrix Algorithm).

Figure 14 shows the computational domain used in the numerical simulation. Level set formulation is used to track the interface. The following mathematical derivations have been taken from Son *et al.* (1999) and Son and Dhir (1998). The level-set function, ϕ, is defined as the signed distance function from the interface. The negative sign is chosen for the vapor phase and the positive sign for the liquid phase. The distance function ϕ is zero at the interface separating the two phases. The shape of the growing bubble is tracked by noting the zero level-set. The governing equations of mass, momentum and energy for the vapor-liquid region can be formulated as,

$$\nabla \cdot \vec{u} = \frac{\vec{m}}{\rho^2} \cdot \nabla \rho + \dot{V}_{micro} \tag{1}$$

$$\rho(\vec{u}_t + \vec{u} \cdot \nabla \vec{u}) = -\nabla p + \rho \vec{g} - \rho \beta_T (T - T_{sat}) \vec{g} - \sigma \kappa \nabla H + \nabla \cdot \mu \nabla \vec{u} + \nabla \cdot u \nabla \vec{u}^T \tag{2}$$

$$\begin{aligned} \rho c_{pl}(T_t + \vec{u} \cdot \nabla T) &= \nabla \cdot \kappa \nabla T \quad \text{for } H > 0 \\ T &= T_{sat} \qquad\qquad \text{for } H = 0 \end{aligned} \tag{3}$$

$$\vec{m} = \rho_l(\vec{u}_{\text{int}} - \vec{u}_l) = \rho_v(\vec{u}_{\text{int}} - \vec{u}_l)$$
$$\rho = \rho_v + (\rho_l - \rho_v)H$$
$$k^{-1} = k_l^{-1} H$$
$$\mu^{-1} = \mu_v^{-1} + \left(\mu_l^{-1} - u_v^{-1}\right)H$$
$$\vec{u}_{\text{int}} = \vec{u} + \vec{m}/\rho$$

$$H = \begin{cases} 1, & \phi \geq +1.5h \\ 0, & \phi \leq +1.5h \\ 0.5 + \phi/3h + \sin[2\pi\phi/3h]/(2\pi), & |\phi| \geq +1.5h \end{cases}$$

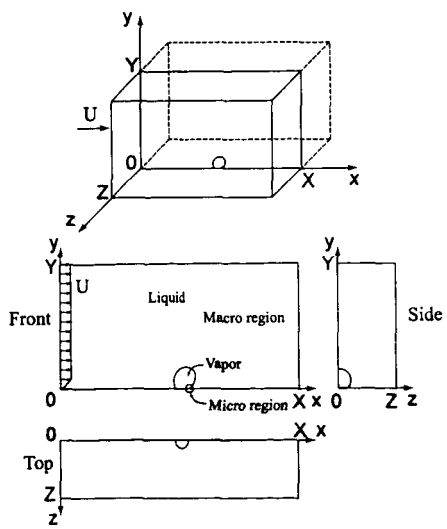

Figure 14: Computational Domain Used in the Numerical Simulation

The level-set function ϕ is advanced at the rate of the interfacial velocity $\vec{u}_{\text{int}}$ and is reinitialized as,

$$\phi_t + \vec{u}_{\text{int}} \cdot \nabla\phi = 0 \tag{4}$$

$$\phi_\tau = \frac{u_0\phi_0}{\sqrt{\phi_0^2 - h^2}\left(1 - |\nabla\phi|\right)} \tag{5}$$

$$\phi_\tau = \frac{u_0(V - V_0)}{V_0}|\nabla\phi| \tag{6}$$

where ϕ_0 is a solution of Eq. (4), τ is an artificial time. To eliminate volumn loss effects, Eq. (6) is added to the whole calculation procedure, where V is the bubble volume and V_0 is the bubble volume which should satisfy mass conservation. Generally speaking, bubble volume, V, calculated from Eq. (5) is smaller than the volume of the bubble, V_0, because of the numerical discretization in the level set formulation. By solving Eq. (6) to attain steady state, the bubble volume V increases to V_0 which gurantees mass conservation at every time step.

The boundary conditions for the governing equations are as follows:

$$\begin{aligned}
&u = u_{in}(y), v = 0, w = 0, T = T_{in}(y), \phi_x = 0 && \text{at} \quad x = 0\\
&u = 0, v = 0, w = 0, T = T_w, \phi_y = -\cos\varphi && \text{at} \quad y = 0\\
&u_z = 0, v_z = 0, w_z = 0, T_z = 0, \phi_z = 0 && \text{at} \quad z = 0\\
&u_x = 0, v_x = 0, w_x = 0, T_x = 0, \phi_x = 0 && \text{at} \quad x = X\\
&u_y = 0, v = 0, w_y = 0, T_y = 0, \phi_y = 0 && \text{at} \quad y = Y\\
&u_z = 0, v_z = 0, w_z = 0, T_z = 0, \phi_z = 0 && \text{at} \quad z = Z
\end{aligned} \tag{7}$$

where φ is the dynamic contact angle, $u_{in}(y)$ and $T_{in}(y)$ are the velocity and temperature profiles at the inlet respectively. In order to capture the flow and temperature field surrounding the bubble, the computational domain is moved with the bubble sliding velocity. The contact angle variation at the bubble base is shown in Fig. 15. At any time step, we use a smoothed function to get the dynamic contact angle φ along the bubble base according to β, which is the angle with respect to the center line.

The simulations are carried out on a uniform grid ($\Delta x = \Delta y = \Delta z$). All simulations consider only half of the bubble, exploiting the planar symmetry of the geometry. The initial thermal boundary layer thickness, is evaluated from the turbulent boundary layer heat transfer correlation given in Kays and Crawford (1980) as,

$$Nu_x = 0.0287 Re_x^{0.8} Pr^{0.6}$$

where $x = 0.15$ m, which is the distance from the inlet to the cavity in the experiments of Maity (2000). After δT is obtained, hydrodynamic boundary layer thickness is calculated from the expression $\delta/\delta T = 1.026\, Pr^{1/3}$.

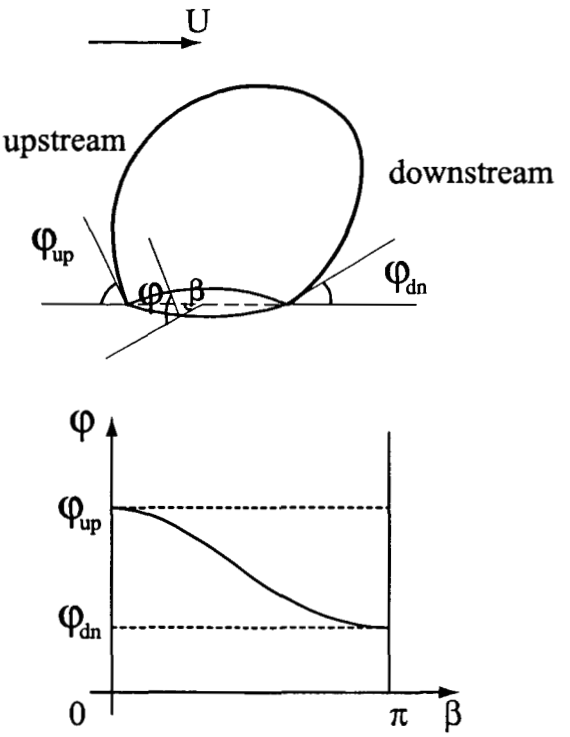

Figure 15: Dynamic Contact Angle Along the Bubble Base.

The initial temperature and velocity profiles are written as,

$$\frac{u_{in}}{U} = \left(\frac{y}{\delta}\right)^{1/7} \tag{8}$$

$$\frac{T_{in} - T_{sat}}{T_w - T_{sat}} = 1 - \left(\frac{y}{\delta_T}\right)^{1/7} \tag{9}$$

During the computations, time steps are small enough to satisfy the CFL condition.

The volume expansion due to microlayer evaporation is added using the model by Son *et al.* (1999).

2.2.1 Results

The length scale and velocity scale are defined as $\ell_0 = \sqrt{\sigma / g(\rho_\ell - \rho_v)}$ and $u_0 = \sqrt{g\ell_0}$, respectively during numerical simulations. All the physical properties are evaluted for saturated water at one atmosphere pressure. Using these properties, the characteristic length scale is 2.5 mm. Numerical simulations were first conducted for vertical upflow case. The wall superheat and bulk flow velocity were taken to be 5 K and 0.076 m/s, respectively. These values were chosen so that the numerical results could be compared with the available experimental data.

The definition of sliding velocity and dependence of contact angle on sliding velocity is given in Fig. 16. Data for the contact angle was reduced from video pictures of Maity [6] and a best fit to the data was obtained. It can be seen that the upstream contact angle initially increases but becomes small when the bubble sliding velocity is high. We consider the contact angle to be advancing when it slides over the vapor region, otherwise it is considered to be the receding contact angle. The contact line velocity is positive when the corresponding contact angle is the receding contact angle, otherwise the contact line velocity is negative. The large scattering in data is a result of ambiguity of the image quality and the uncertainty in the measurements. However, the upstream contact angle decreases sharply when the velocity increases to about 0.1 *m/s*. After that, there is not much difference between upstream and downstream contact angles. This is probably because the contact line drags some liquid underneath the bubble when the contact line velocity is high enough. Hence there may be a liquid layer present between the bubble and the heating surface. This causes the dynamic contact angle on the upstream side to be small. The best fit of the contact angle was used as an input to the numerical model.

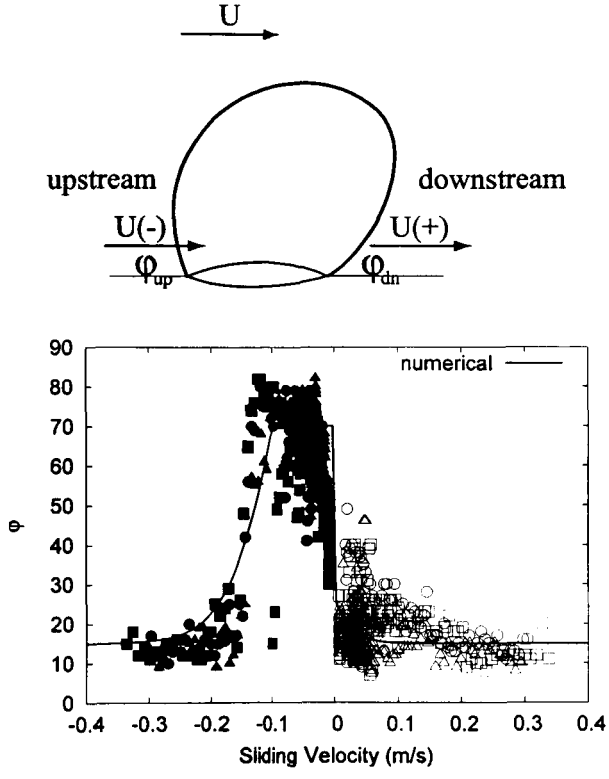

Figure 16: (a) The Definition of Sliding Velocity; (b) Dynamic Contract Angle as a Function of Sliding Velocity.

The bubble shape, observed in the experiments and numerical simulation, during one growth cycle is shown in Fig. 17. Figure 18 shows the velocity field in and around the bubble as obtained from numerical simulations. During the early period of bubble growth, the bubble shape is almost spherical because of the surface tension force. As the bubble grows and begins sliding, the bubble becomes elongated in the direction normal to the heating surface, resulting in elliptical bubbles. Also the bubble base diameter changes as it slides and when the bubble base reduces to zero, the bubble lifts off from the surface. For the vertical flow boiling case, the gravity direction is parallel to the heating surface so there is no lift off force due to gravity.

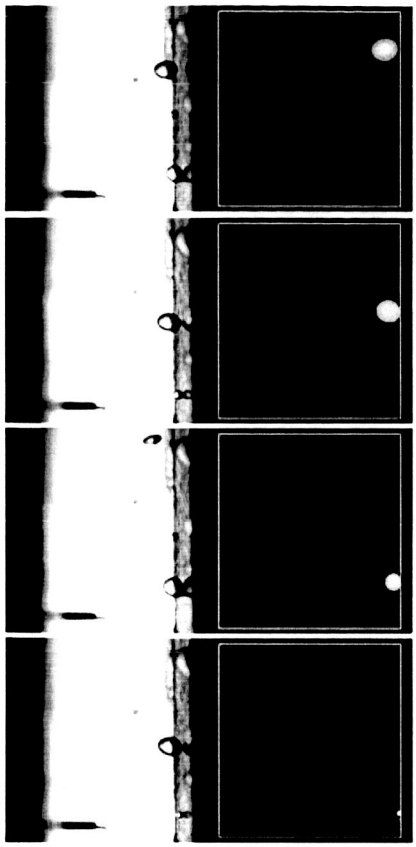

Figure 17: Comparison of Bubble Shape with Experimental Data (vertical surface, U = 0.076 m/s, ΔT = 5.0 K).

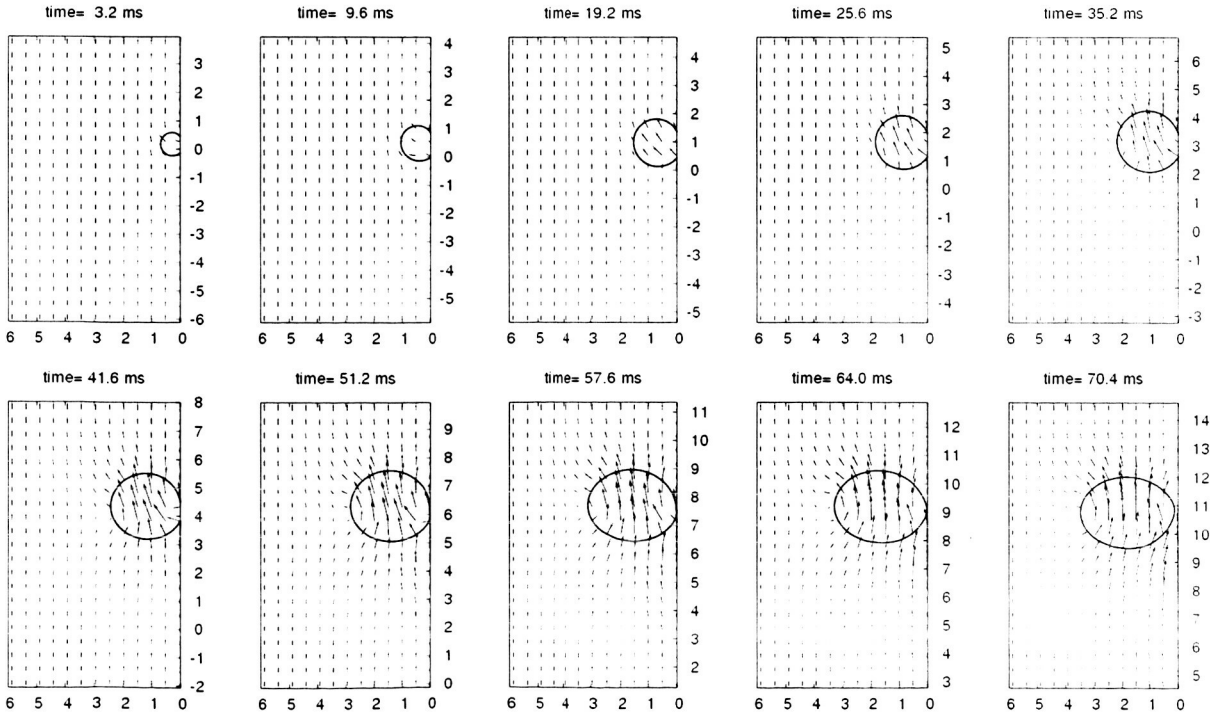

Figure 18: Velocity Field During Bubble Growth, Sliding and Lift Off (vertical surface, U = 0.076 m/s, ΔT = 5.0 K).

Figure 19 shows the temperature field around the bubble. As the bubble slides, the thermal layer behind the bubble become thicker, but the temperature gradient near the heating surface under and surrounding the bubble increases. This in turn corresponds to an increase in heat flux.

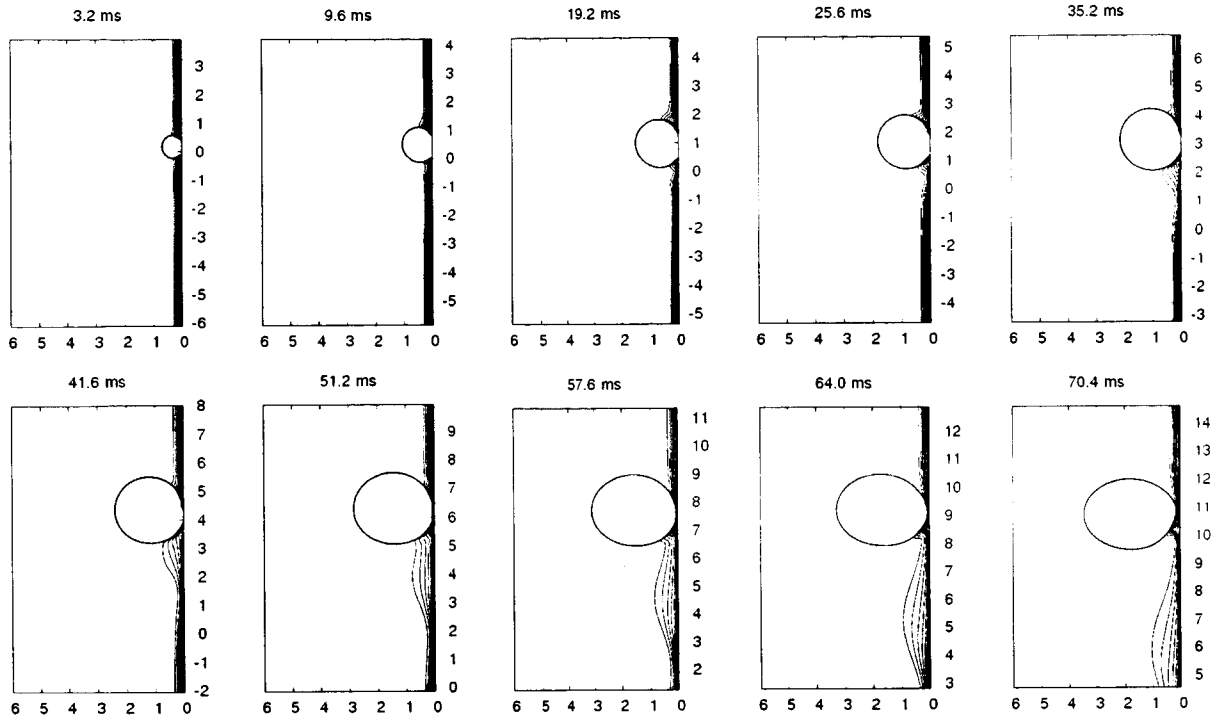

Figure 19: Temperature Field with Temperature Interval of 0.5 K (vertical surface, U = 0.076 m/s, ΔT = 5.0 K).

Figure 20 shows the comparison of bubble growth and sliding distance between numerical simulation and experimental data. It can be seen that the numerical results somewhat overpredict the bubble diameter at departure, growth period and sliding distance.

Figure 21 shows the pressure contours when the bubble is about to lift off. The pressure on the top of the bubble is smaller than the pressure at the bubble base. As a result of this pressure difference the bubble lifts off normal to the gravity vector.

The model was applied to surfaces at 45, 30 to the gravity vector. Figures 22 and 23 show the numerical results for the two cases respectively. In both cases, the numerical predictions for bubble growth, bubble diameter at lift-off and bubble sliding distance are found to be in reasonable agreement with the experimental data. The magnitude of gravity normal and parallel to the heater surface changes with the orientation of heater surface. This has an effect on bubble lift off time. The normal component of gravity decreases with increase in angle of inclination. Thus, the contribution of buoyancy becomes smaller when angle of inclination is increased. As a result, the bubble needs to grow to a bigger size to get enough lift to detach from the surface.

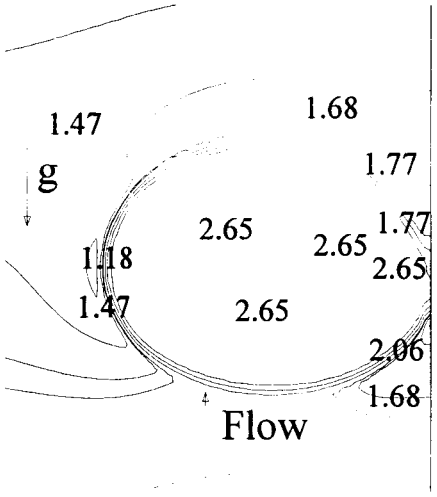

Figure 21: The Nondimensional Pressure Contour Near the Bubble When the Bubble is Almost at Lift Off (vertical surface, U = 0.076 m/s, ΔT = 5.0 K).

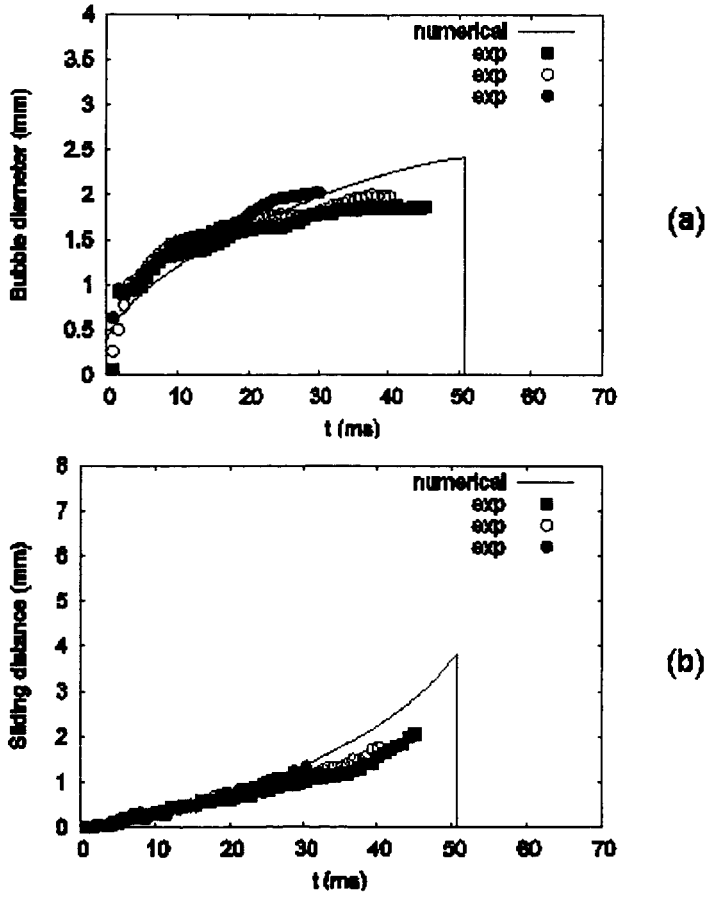

Figure 22: Comparison of (a) Bubble Diameter, and (b) Bubble Sliding Distance Predicted from Liquid Layer Model with Experimental Data (45° inclined surface, U = 0.076 m/s, ΔT = 5.0 K).

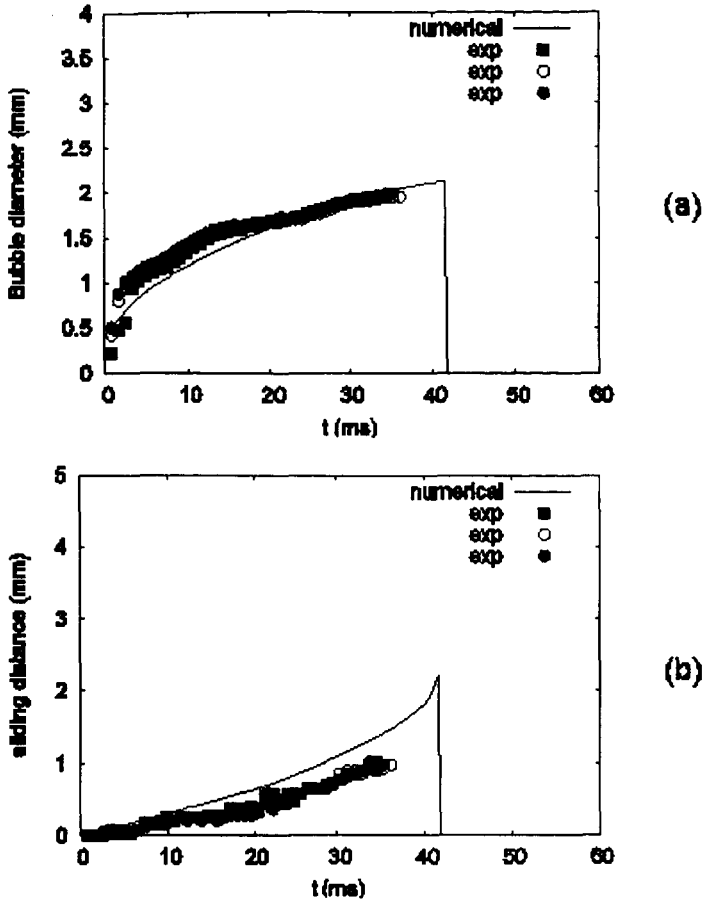

Figure 23: Comparison of (a) Bubble Diameter, and (b) Bubble Sliding Distance Predicted from Liquid Layer Model with Experimental Data (30° inclined surface, U = 0.076 m/s, ΔT = 5.0 K).

REFERENCES

Kays, W. M., and Crawford, M. E., 1980. *Convective Heat and Mass Transfer.* McGraw-Hill, New York.

Son, G., Dhir, V. K., and Ramanujapu, N., 1999. "Dynamics and Heat Transfer Associated with a Single Bubble During Nucleate Boiling on a Horizontal Surface". *Journal of Heat Transfer,* **121**, pp. 623–631.

Son, G., and Dhir, V. K., 1998. "Numerical Simulation of Film Boiling Near Critical Pressures with a Level Set Method". *Journal of Heat Transfer,* **120**, pp. 183–192.

Von Arx, A.R. and Dhir, V.K., 1993. "System Simulation of a Thermionic Reactor," Paper No. 93-HT-24, presented at the National Heat Transfer Conference, Atlanta, GA.